PAPER

Development of CMOS-MEMS in-plane magnetic coils for application as a three-axis resonant magnetic sensor

IOP Publishing Journal of Micromechanics and Microengineering
J. Micromech. Microeng. **24** (2014) 035016 (14pp) doi:10.1088/0960-1317/24/3/035016

Development of CMOS-MEMS in-plane magnetic coils for application as a three-axis resonant magnetic sensor

Chun-I Chang[1], **Ming-Han Tsai**[2], **Chih-Ming Sun**[2] **and Weileun Fang**[1,3]

[1] Institute of NanoEngineering and MicroSystems, National Tsing Hua University, Hsinchu, Taiwan
[2] PixArt Imaging Inc., Hsinchu, Taiwan
[3] Power Mechanical Engineering, National Tsing Hua University, Hsinchu, Taiwan

E-mail: fang@pme.nthu.edu.tw

Received 1 November 2013, revised 14 January 2014
Accepted for publication 14 January 2014
Published 28 February 2014

Abstract

This study designs and implements a single unit three-axis magnetic sensor using the standard TSMC 0.35 μm 2P4M CMOS process. The magnetic sensor consists of springs, a proof-mass with embedded magnetic coils, and sensing electrodes. Two sets of in-plane magnetic coils respectively arranged in two orthogonal axes are realized using the stacking of metal and tungsten layers in the CMOS process. The number of turns for the proposed in-plane magnetic-coil is not restricted by the space and thin film layers of the CMOS process. The magnetic coils could respectively generate Lorentz and electromagnetic forces by out-of-plane and in-plane magnetic fields to excite the spring–mass structure. Capacitance sensing electrodes could detect the dynamic response of the spring–mass structure to determine the magnetic fields. Measurements indicate the typical sensitivities of the sensor are 0.21 μV μT^{-1} (x-axis), 0.20 μV μT^{-1} (y-axis), and 0.90 μV μT^{-1} (z-axis) at 1 atm. Moreover, the resolutions of the sensor are respectively 384 nT rtHz^{-1} for the x-axis, 403 nT rtHz^{-1} for the y-axis, and 62 nT rtHz^{-1} for the z-axis at 1 atm. The presented magnetic sensor could monolithically integrate with other CMOS-MEMS devices for various applications.

Keywords: three-axis resonant magnetic sensor, in-plane magnetic coils, CMOS-MEMS

(Some figures may appear in colour only in the online journal)

1. Introduction

Presently, smart phones are generally equipped with three-axis magnetic sensors for personal navigation applications. Thus, the demand for three-axis magnetic sensors is significantly increased. Magnetoresistive (MR) [1] and Hall-effect magnetic sensors [2] are the dominant technologies used in the existing electronic compasses [3]. The Hall-effect magnetic sensors can be realized using the standard CMOS process, and no special magnetic materials are required. On the other hand, the MR magnetic sensor has a higher sensitivity. The resonant-type magnetic sensors with suspended MEMS (micro-electro-mechanical systems) structures have been extensively investigated [4–12]. The resonant-type magnetic sensor has a high resolution and low power consumption [6–8]. Moreover, the resonant-type magnetic sensor can be implemented using various existing MEMS processes, and thus has the potential to monolithically integrate with other MEMS sensors such as accelerometers and gyroscopes for different applications.

The Lorentz force induced by a magnetic field could deform the suspended MEMS structures with small stiffness. Thus, the deformation of MEMS structures has been exploited to measure the magnetic fields. The three-axis magnetic fields are detected by the deformation of three discrete micromachined cantilevers with embedded piezoresistive sensors [9]. The suspended MEMS structure will experience a periodic Lorentz force in a magnetic field when there is an input from an ac current [4]. The dynamic responses of MEMS structures can be exploited to determine the magnetic fields. In this design, the resonant vibration of the MEMS

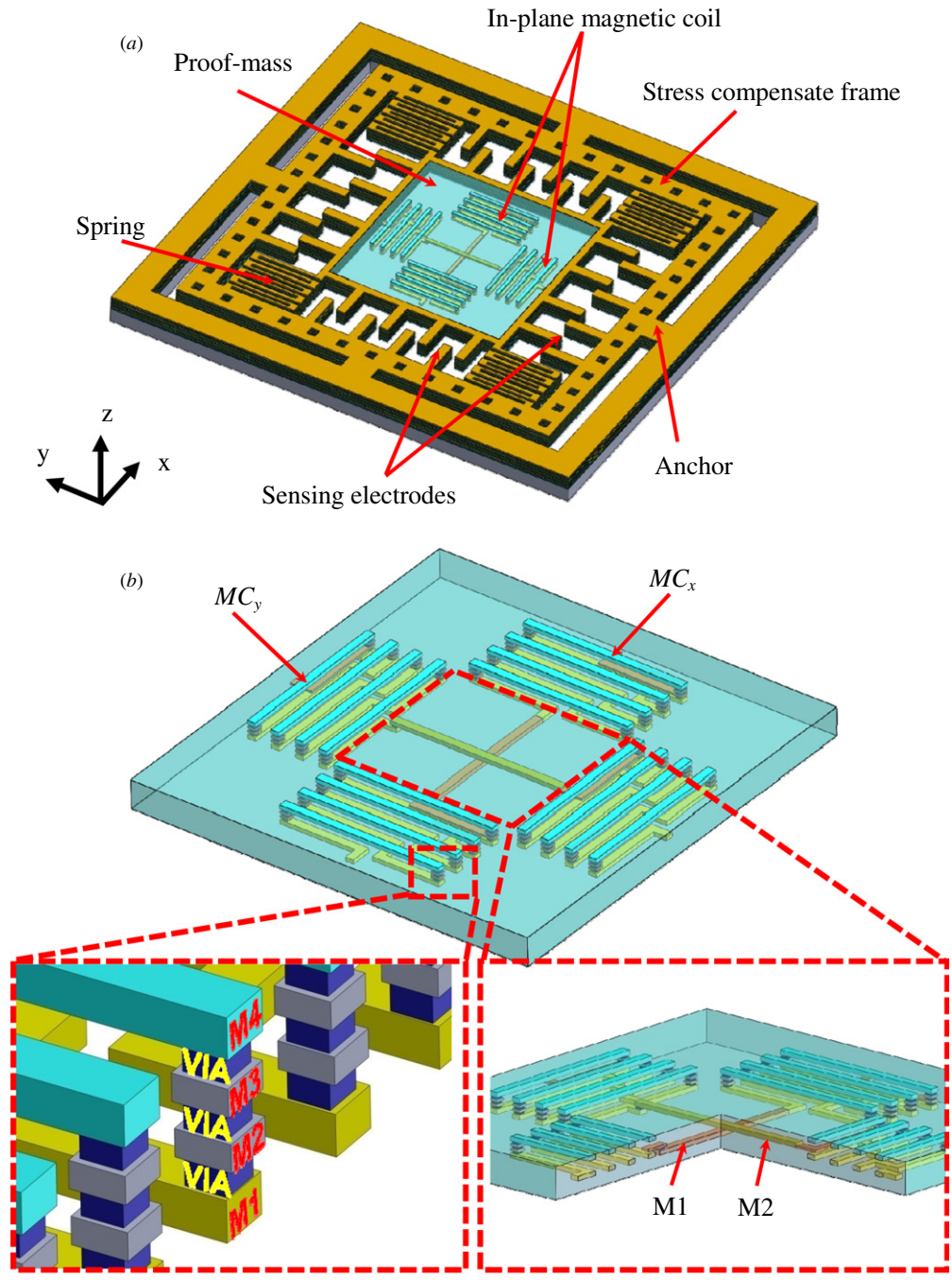

Figure 1. The schematic design of the present three-axis magnetic sensor: (*a*) the magnetic sensor consists of a proof-mass with embedded magnetic coils, springs, sensing electrodes and stress compensation frame, and (*b*) the in-plane magnetic coils and their electrical routings are formed by the stacking of metal and tungsten layers for CMOS processes.

structure is frequently employed to magnify the dynamic response. The existing resonant-type magnetic sensors are mainly designed to detect single-axis magnetic fields. Thus, three separate resonant-type sensing units are integrated to detect the three-axis magnetic fields for electronic compass application [6]. In general, the out-of-plane magnetic field could easily introduce an in-plane excitation and dynamic response on the suspended MEMS structure by the Lorentz force. Thus, it is easier to detect the out-of-plane magnetic field by using the resonant-type sensor. A single MEMS structure enabling the measurement of two-axis magnetic fields is reported in [8].

The CMOS-MEMS sensors have the advantages of using an existing foundry service, electrical routing compatibility and monolithic integration of MEMS structures and sensing circuits [10]. The resonant-type magnetic sensors of different micromachined structure designs have been demonstrated using the CMOS-MEMS processes [11, 12]. Piezoresistive sensing has been employed to measure the dynamic response of the MEMS structures. The in-plane magnetic coil fabricated

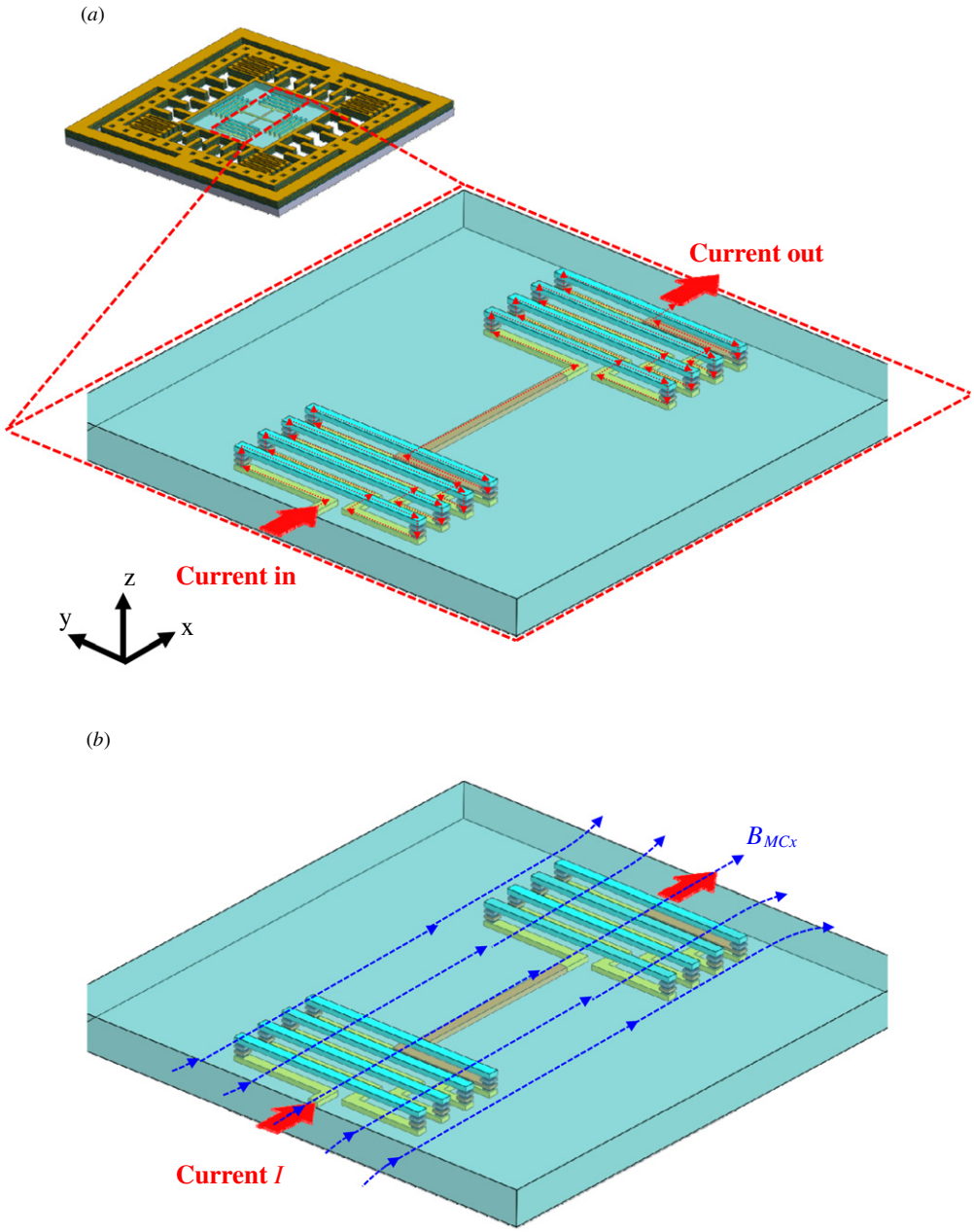

Figure 2. The schematic illustrations show (*a*) the current input into the in-plane magnetic coil MC_x, and (*b*) the electromagnetic field B_{MCx} generated by the magnetic coil MC_x after the current is input.

using the standard CMOS process has been reported in [13]. The Lorentz and electromagnetic forces will be induced by the magnetic fields to excite the suspended MEMS structures. The two-axis magnetic fields are thus detected by the dynamic responses of MEMS structure. However, the integration of two discrete sensing units is required for the detection of three-axis magnetic fields. The presented study takes the advantages of the CMOS process and further extends the concept in [13] to develop a CMOS-MEMS resonant-type magnetic sensor with two in-plane coils for the detection of three-axis magnetic fields. In this study, a single unit three-axis magnetic sensor using the standard TSMC 0.35 μm 2P4M CMOS process has been designed and demonstrated. In short, the present design has the following advantages: (1) the number of turns for the in-plane magnetic-coil is not restricted by the space and thin film layers of the CMOS process, (2) the integration of two in-plane magnetic-coils enables the detection of three-axis magnetic fields using a single sensing unit, and (3) it can further monolithically integrate with other CMOS-MEMS devices for different applications.

2. Design concept

Figure 1 illustrates the schematic design of the present three-axis magnetic sensor. The sensor is designed based on the standard TSMC 0.35 μm 2P4M process. As indicated in figure 1(*a*), the magnetic sensor consists of a proof-mass with embedded magnetic coils, springs, sensing electrodes and stress compensation frame. The zoom-in illustration in

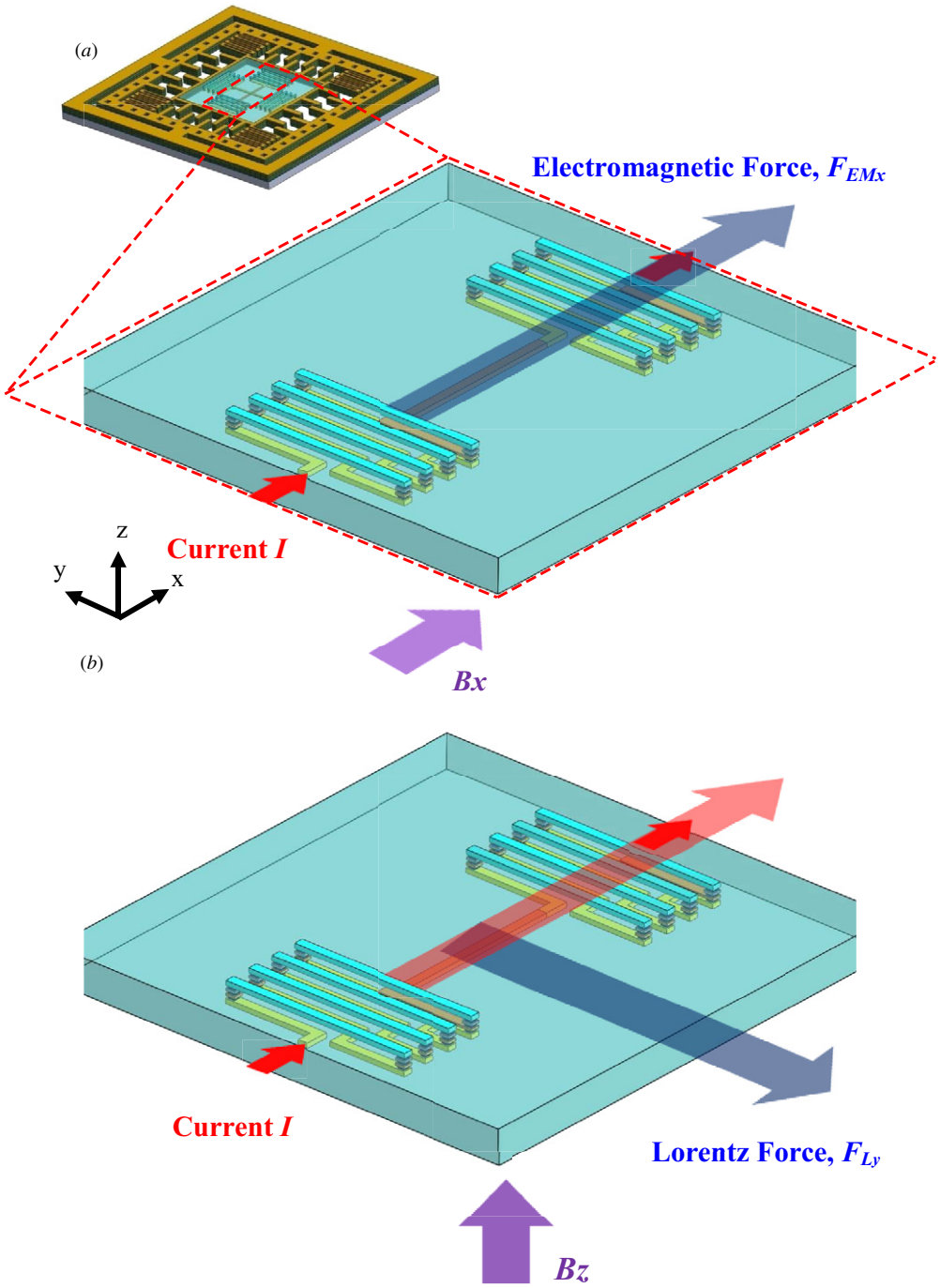

Figure 3. As the current is input into the in-plane magnetic coil MC_x, (*a*) the electromagnetic force in the *x*-axis F_{EMx} will be induced by the magnetic field B_x, and (*b*) the Lorentz force in the *y*-axis F_{Ly} will be induced by the magnetic field B_z.

figure 1(*b*) further shows that the concept of an oxide-rich CMOS-MEMS structure in [14] is employed to design the proof-mass. Two sets of in-plane magnetic coils (MC_x and MC_y) are embedded in the proof-mass. The left inset depicts the in-plane magnetic coils consisting of the stacked conductive films in the standard 2P4M process, including four metal layers (as labeled in M1–M4) and tungsten vias. As indicated in the right inset, the M1 and M2 metal layers are respectively employed to act as the central electrical routings for these two sets of magnetic coils. As shown in figure 2, these two sets of in-plane magnetic coils are designed to respectively provide two in-plane magnetic fields (B_{MCx} and B_{MCy}) in orthogonal directions after applying currents. Figure 2(*a*) shows the input current *I* for magnetic coil MC_x. As shown in figure 2(*b*), the magnetic field B_{MCx} is generated by the in-plane magnetic-coil MC_x after the current input into the coil. Similarly, the input current on the magnetic-coil MC_y will introduce the magnetic field B_{MCy}. According to the

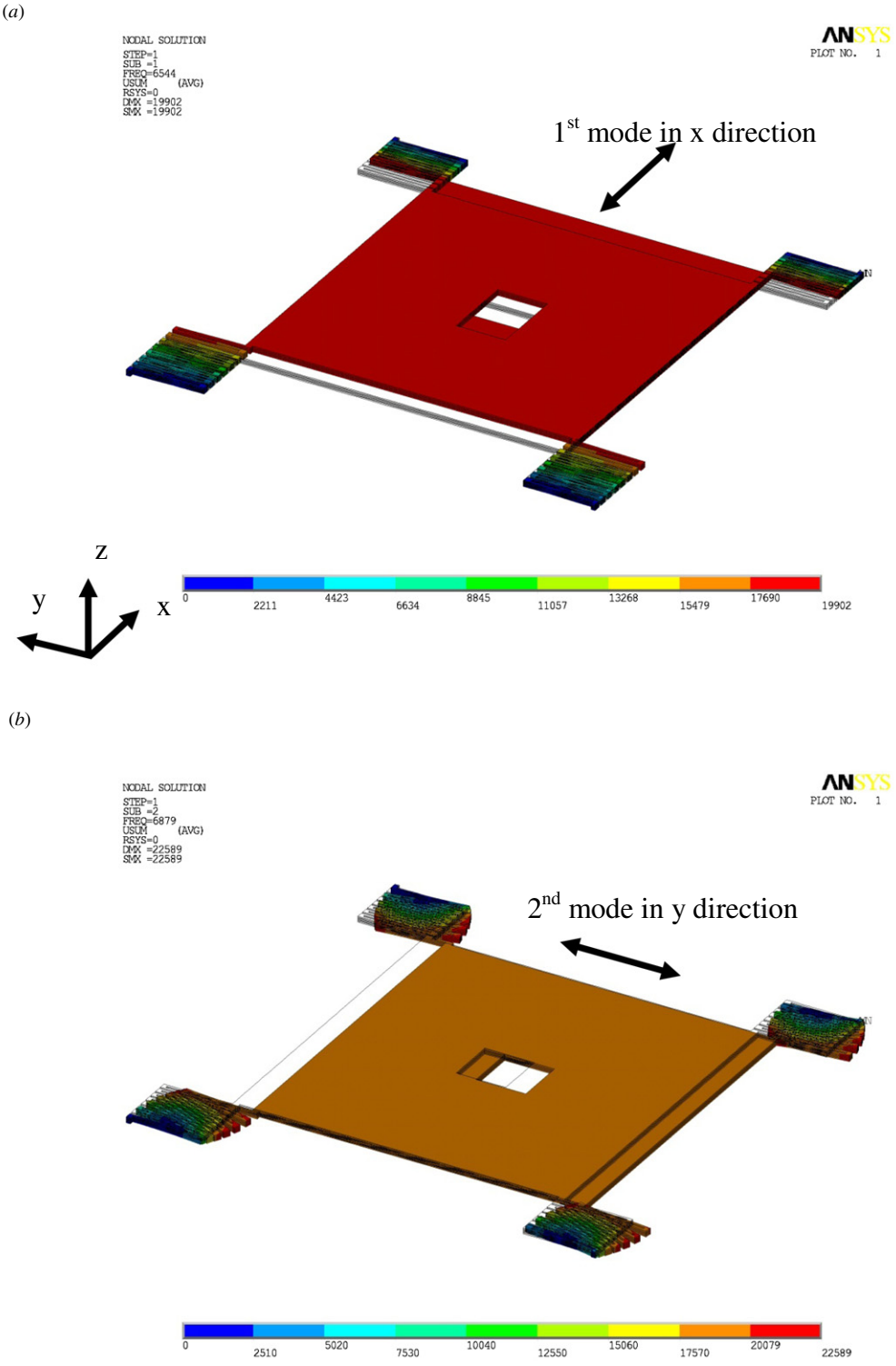

Figure 4. The first two vibration modes of typical spring–mass design predicted by the FEM simulation: (*a*) the first mode has oscillations in the *x*-axis direction, and (*b*) the second mode has oscillations in the *y*-axis direction.

magnetic field B_{MCx} (or B_{MCy}) introduced by the magnetic coil, the electromagnetic force F_{EMx} (or F_{EMy}) will apply on the proof-mass when the sensor is exposed to the magnetic field B_x (or B_y), as indicated in figure 3(*a*).

The force F_{EMx} (or F_{EMy}) in figure 3(*a*) is proportional to magnetic fields B_x (or B_y) at a given input current. When applying an ac current of frequency ω_1 to the magnetic-coil MC_x in magnetic field B_x, the loading and response on proof-mass M of the sensor can be expressed as,

$$M\ddot{X} + C_x\dot{X} + K_xX = F_{EMx}\sin\varpi_1 t \quad (1)$$

where C_x and K_x are respectively the equivalent damping coefficient and the stiffness of the sensor in the *x*-axis. The dynamic response X of the proof-mass in equation (1) can be expressed as

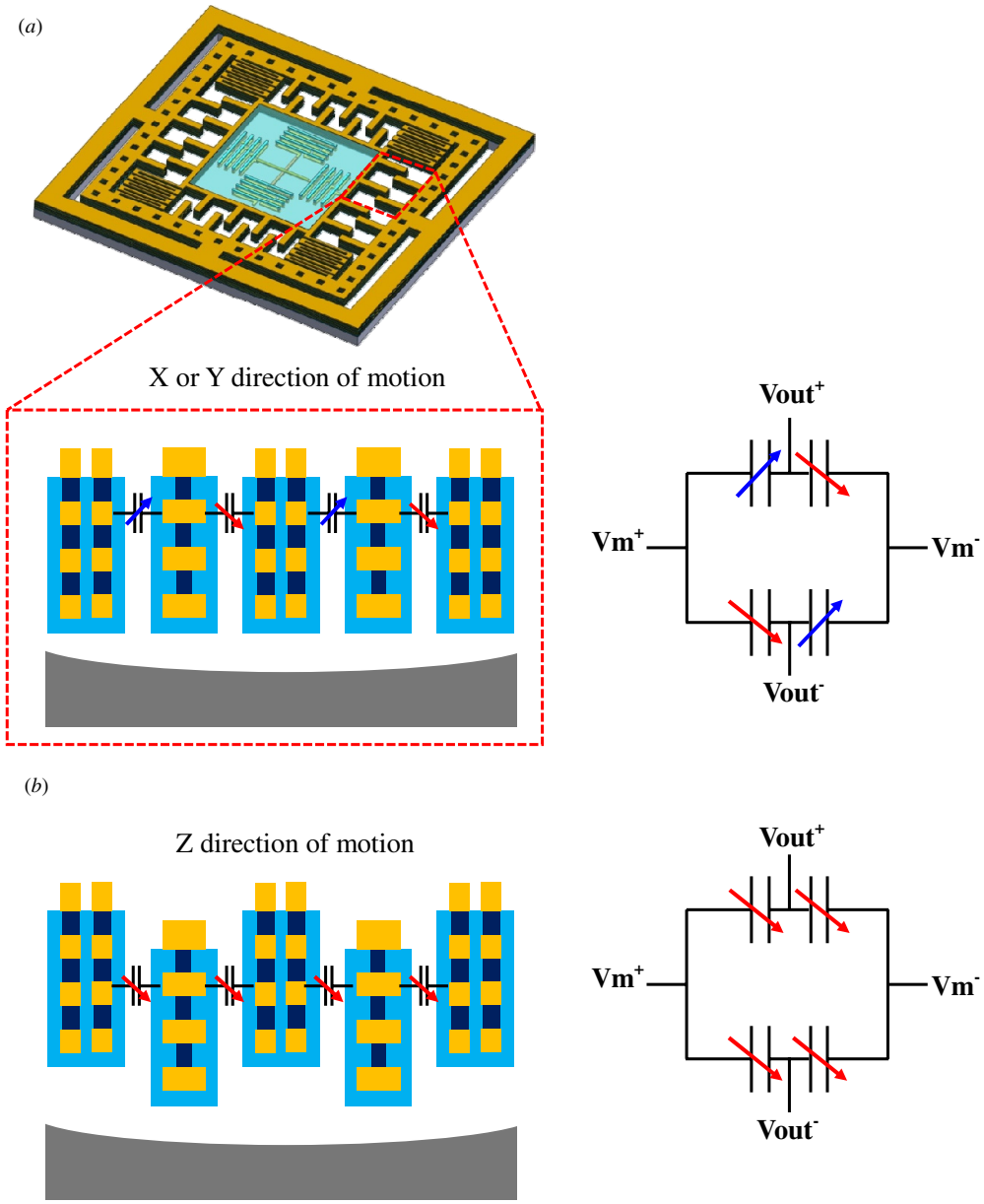

Figure 5. A fully differential sensing circuit for (*a*) in-plane motion, and (*b*) out-of-plane motion.

$$X = X_0 \sin(\varpi_1 t - \phi), \qquad \phi = \tan^{-1} \frac{C_x \varpi_1}{K_x - M\varpi_1^2} \tag{2}$$

where X_0 is the steady state vibration amplitude of the proof-mass, and can be further expressed as,

$$X_0 = \frac{F_{\mathrm{EM}x}}{\sqrt{\left(K_x - M\varpi_1^2\right)^2 + (C_x \varpi_1)^2}}. \tag{3}$$

As indicated in equation (3), the vibration amplitude is proportional to the electromagnetic force $F_{\mathrm{EM}x}$. Thus, the magnetic field B_x can be determined by the vibration amplitude X_0. As shown in figure 1(*a*), the vibration amplitude X_0 can be detected by the capacitance sensing electrodes. Moreover, according to equation (3), the vibration amplitude and the sensing capacitance can be further increased when operating the spring–mass system in its natural frequency. In other words, the frequency ω_1 of the input ac current is the same as the natural frequency of the spring–mass structure ω_x. The design considerations in the *y*-axis are the same as those in the *x*-axis.

Figure 3(*b*) depicts the equivalent direction of the input current I in the magnetic coil MC_x. Thus, a Lorentz force F_{Ly} will apply on the proof-mass as the sensor is exposed to the magnetic field B_z:

$$F_{Ly} = L_{\mathrm{eff}} I \times B_z \tag{4}$$

where L_{eff} is the effective length of the magnetic coil for the Lorentz force. Similarly, as applying an ac current of frequency ω_2 to the magnetic-coil MC_x in a magnetic field B_z, the loading and response on the proof-mass M of the sensor can be expressed as,

$$M\ddot{Y} + C_y\dot{Y} + K_y Y = F_{Ly} \sin \varpi_2 t \tag{5}$$

where C_y and K_y are respectively the equivalent damping coefficient and the stiffness of the sensor in the *y*-axis. The steady state vibration amplitude Y_0 of the proof-mass becomes,

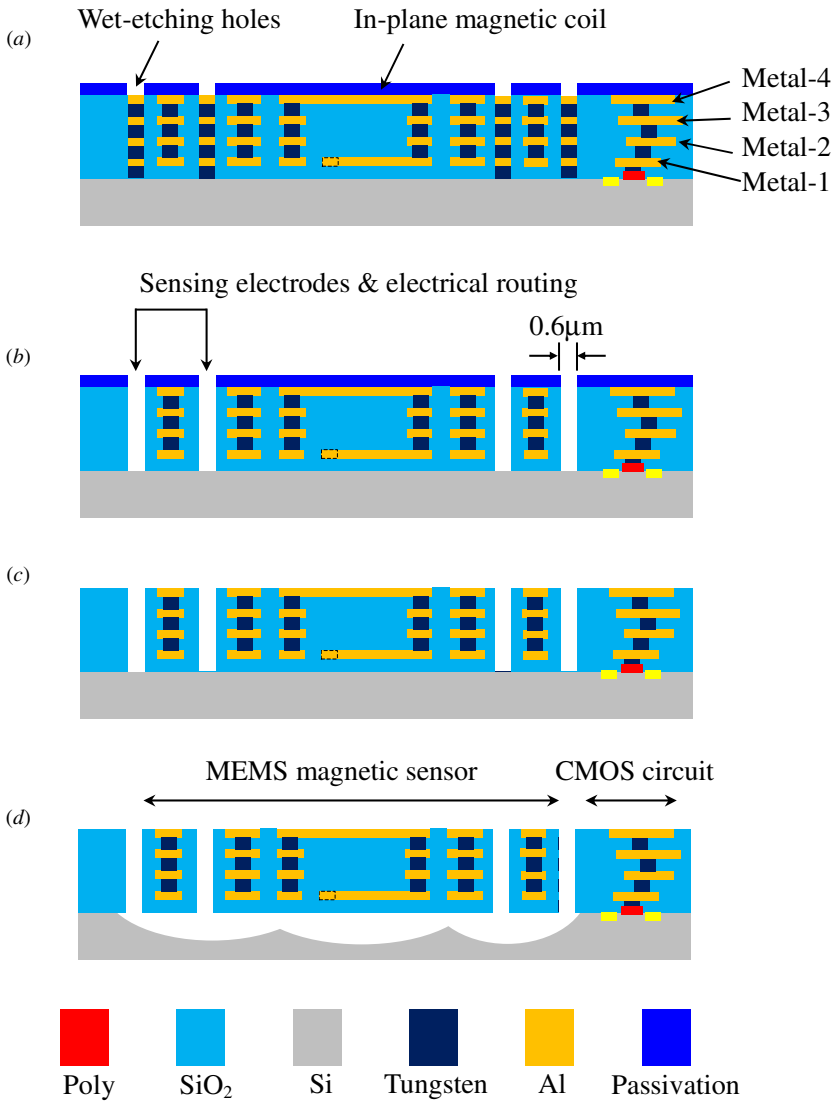

Figure 6. The fabrication process steps.

$$Y_0 = \frac{F_{Ly}}{\sqrt{\left(K_y - M\varpi_2^2\right)^2 + (C_y\varpi_2)^2}}. \quad (6)$$

According to equations (4)–(6), the magnetic field B_z can also be detected by the vibration amplitude Y_0 of the spring–mass system at the given L_{eff} and input current I. In this case, the dynamic response as well as sensing signal is also significantly increased by resonance when the frequency ω_2 of the input ac current agrees with the natural frequency of the spring–mass system ω_y.

In summary, this study designs a spring–mass structure with two in-plane natural frequencies ω_x and ω_y. Figure 4 shows the mode shapes predicted by the finite element method (FEM) for a typical spring–mass design. The first two modes indicated in figures 4(*a*) and (*b*) have oscillations respectively in the *x*-axis and *y*-axis directions. The ac current of two different frequencies ω_x and ω_y is applied into the magnetic coils MC_x during sensing. The periodic electromagnetic forces of frequencies ω_x and ω_y in the direction of the *x*-axis are introduced by the magnetic field B_x. Thus, the vibration amplitude X_0 of frequency ω_x is employed to detect the magnetic field B_x. Since the driving frequency ω_x agrees with the first natural frequency of the spring–mass structure in figure 3(*a*), a larger amplitude X_0 is achieved. Meanwhile, the periodic Lorentz forces of frequency ω_x and ω_y in the direction of the *y*-axis are introduced by the magnetic field B_z. The vibration amplitude Y_0 of frequency ω_y is employed to detect the magnetic field B_y. Similarly, the driving frequency ω_y agrees with the second resonant frequency of the spring–mass structure in figure 3(*b*) and a larger amplitude Y_0 is also achieved. As a result, the in-plane magnetic field B_x and out-of-plane magnetic field B_z are determined by the in-plane vibration amplitudes in two orthogonal directions. By using the same concept, the in-plane magnetic field B_y and out-of-plane magnetic field B_z are detected using the in-plane magnetic coil MC_y. With embedded magnetic coils MC_x and MC_y aligned in two orthogonal directions, the proposed spring–mass structure design in figure 1 can detect the three-axis magnetic field. Thus, the single MEMS sensing unit for three-axis field measurement is achieved.

In the presented magnetic sensor, the fully differential sensing electrodes shown in figure 5(*a*) and their sensing

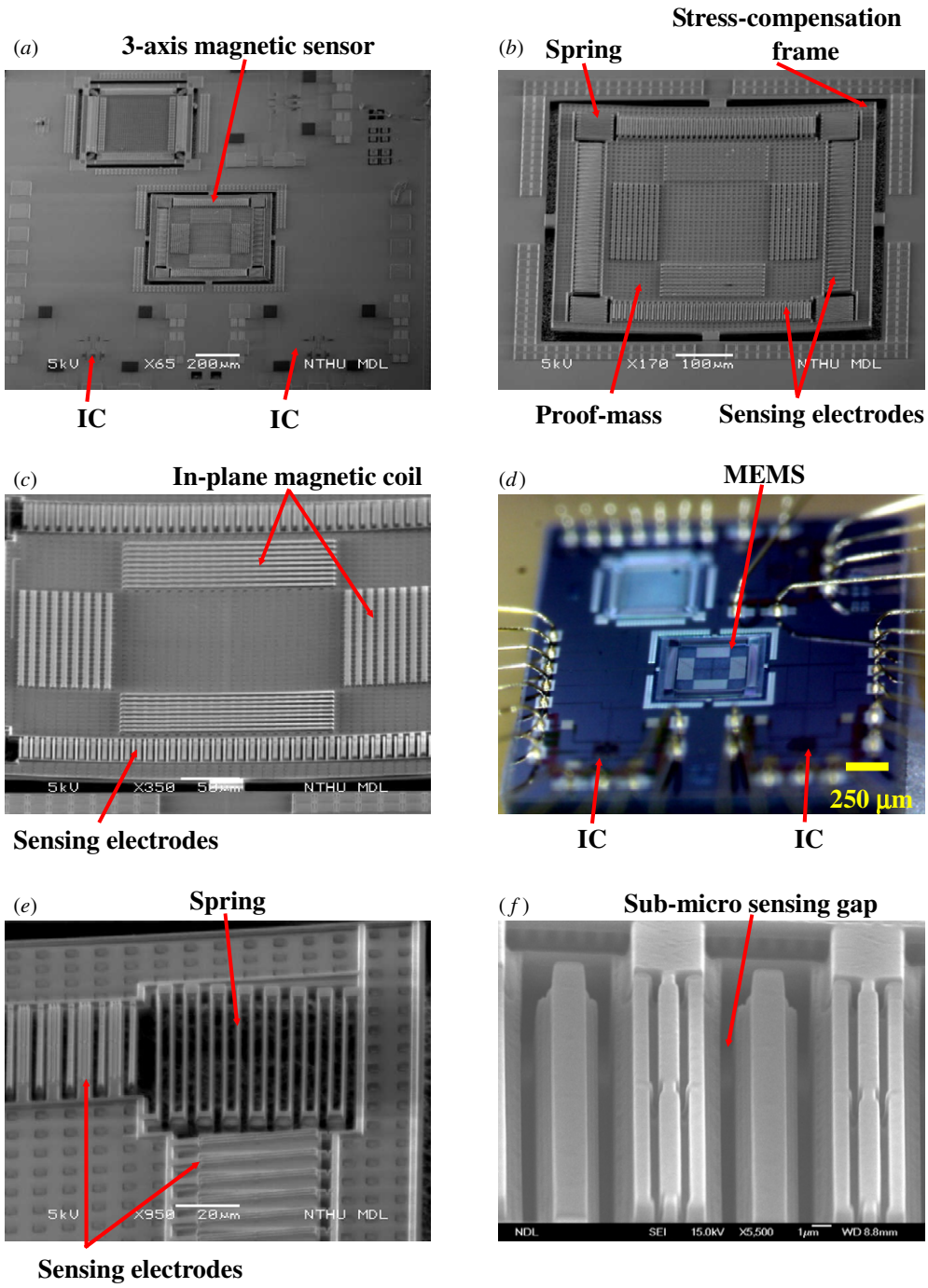

Figure 7. The micrographs of typical fabrication results: (*a*) the chip containing a three-axis magnetic sensor and its monolithically integrated sensing circuits, (*b*) the overview of a 600 μm $\times$ 580 μm suspended structure consisting of springs, proof-mass, stress-compensation frame and sensing electrodes, (*c*) two sets of in-plane magnetic coils embedded in the proof-mass, (*d*) the sensing chip after wire bonding, (*e*) sensing electrodes in two different axes and the spring, and (*f*) the electrodes with sub-micron sensing gap.

circuits are also implemented and integrated using the standard CMOS process. The preamplifier in this study acted as a buffer with a gain (Gain_{amp}) of one. The cross-axis sensitivity and noise performance can be minimized under this condition [15]. For instance, the in-plane magnetic field B_x (or B_y) will generate an out-of-plane (z-axis direction) Lorentz force and further cause an unwanted out-of-plane motion on the proof-mass. The sensing signals induced by such unwanted out-of-plane motion can be canceled using the differential sensing electrodes design, as shown in figure 5(*b*). The detailed design parameters of the proposed magnetic sensor are summarized in table 1. The sensor has a suspended mechanical structure (including spring, mass and stress compensation frame) of 600 μm $\times$ 580 μm, and the footprint of proof-mass is 420 μm $\times$ 420 μm. In this design, the magnetic coil has 18 turns in each direction, and the effective length L_{eff} for the Lorentz force extracted from FEM simulation (ANSOFT Maxwell) is 584 μm. The mechanical characteristics for

(*a*)

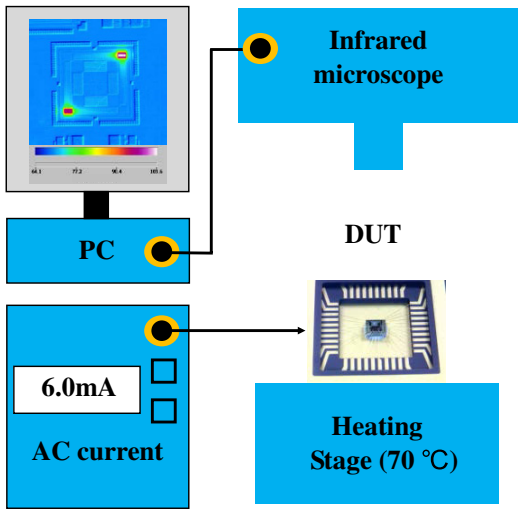

(*b*)

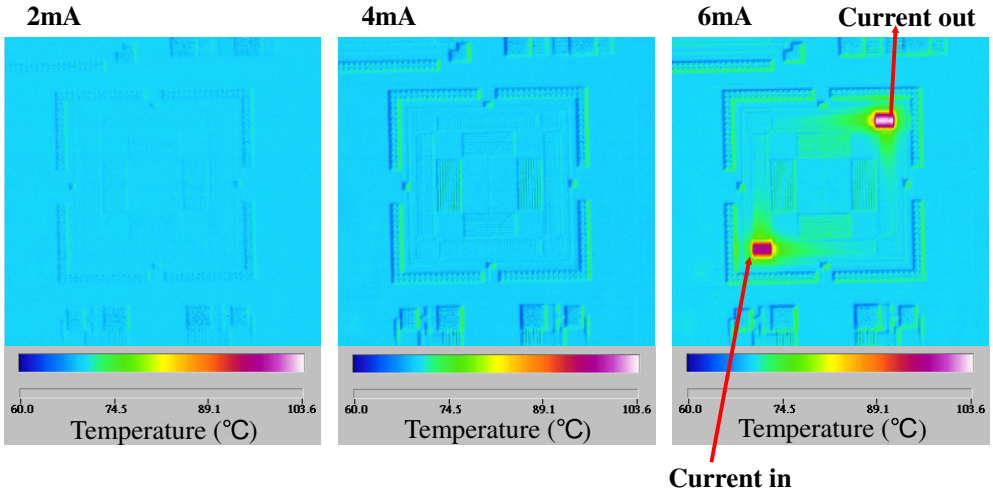

Figure 8. (*a*) The measurement setup to characterize the temperature increase of the structure after applying currents to the magnetic coil, and (*b*) the typical measured temperature distribution displayed by colors as defined in the keys.

Table 1. The typical design parameters of a proposed magnetic sensor.

	Design specifications of the magnetic sensor	
Parameters	Electromagnetic force (X/Y magnetic field)	Lorentz force (Z magnetic field)
MEMS structure size	600 × 580 μm^2	
Proof-mass size	420 × 420 μm^2	
In-plane magnetic coil (turns)	18	–
Effective length (L_{eff})	–	584 μm
Spring stiffness (N m^{-1})	X: 3.73 N m^{-1} Y: 4.79 N m^{-1}	3.73 N m^{-1}
Natural frequency	X: 6.5 kHz Y: 6.8 kHz	6.8 kHz
Initial capacitance (C_o)	154.5 fF	154.5 fF
Capacitance gap	0.6 μm	0.6 μm

sensors have also been predicted by the FEM simulation (ANSYS). The spring stiffnesses in the x-axis and y-axis directions are respectively $K_x = 3.73$ N m^{-1} and $K_y = 4.79$ N m^{-1}. As shown in figure 4, the first two natural frequencies are respectively $\omega_x = 6.5$ kHz (linear vibration in the x-axis with the proof-mass as a rigid body, as shown in figure 3(*a*)) and $\omega_y = 6.8$ kHz (linear vibration in the y-axis with the proof-mass as a rigid body, as shown in figure 3(*b*)).

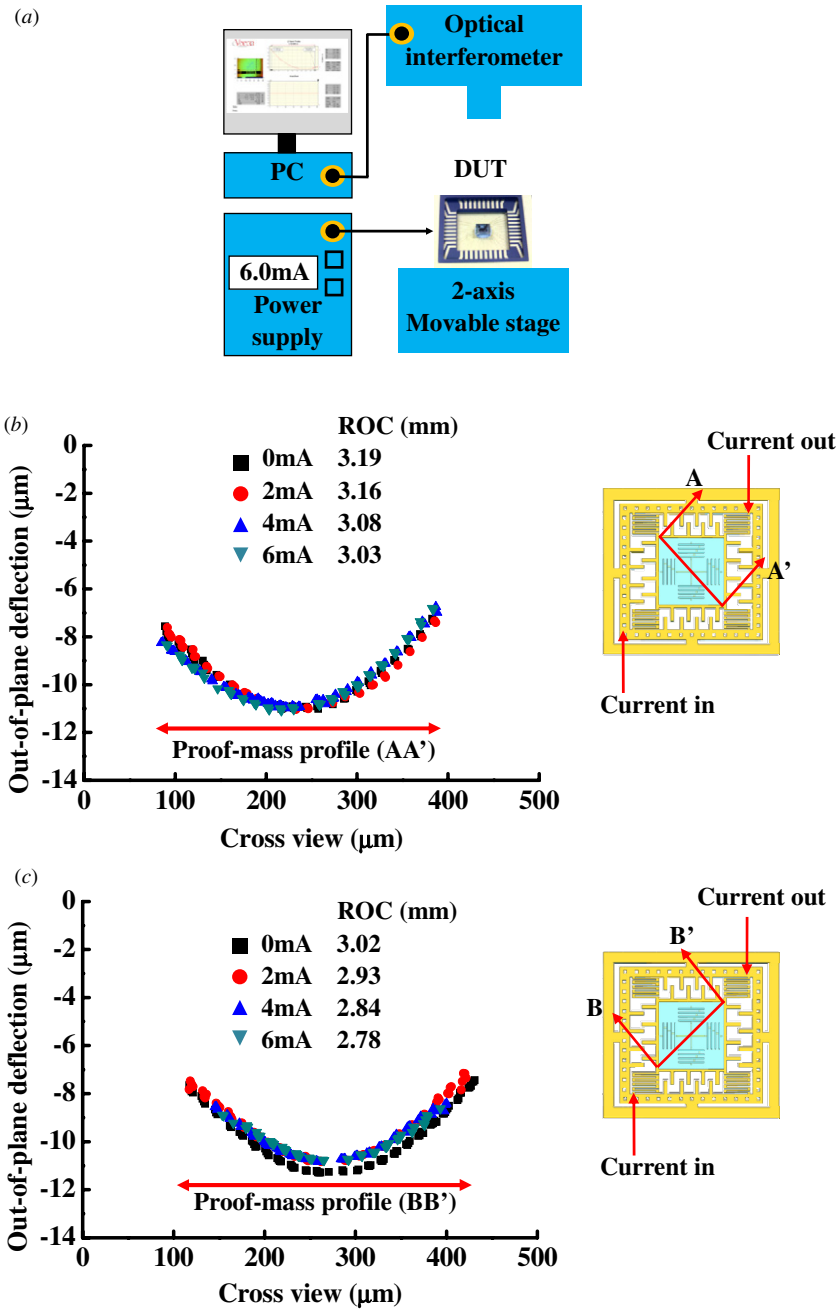

Figure 9. (*a*) The measurement setup to characterize the thermal deformations of the suspended structure, (*b*) and (*c*) the structure deformations respectively characterized along the AA′ and BB′ cross sections at different input currents.

3. Fabrication and results

Figure 6 shows the fabrication process steps to implement the magnetic sensor. Figure 6(*a*) indicates the chip prepared by the standard TSMC 0.35 μm 2P4M CMOS process. After that, the in-house metal wet etching and silicon substrate dry etching were employed to release the suspended MEMS structures. The etching solution with H_2SO_4 and H_2O_2 was used to remove the metal and tungsten-via sacrificial layers [16]. After that, the in-plane shapes of the MEMS structures, such as the springs, proof-mass, sensing electrodes and sensing gaps, were defined, as indicated in figure 6(*b*). During the wet etching process, the metal films for magnetic coils, sensing electrodes and electrical routings were protected by the surrounding dielectric layers of the CMOS process. In addition, the minimum line width of metal and tungsten vias for CMOS process properly defined and implemented the sub-micron in-plane sensing gaps. Note that the MEMS structures with submicron sensing gaps were not suspended during the wet etching process. Thus, the stiction problems that frequently occur during the wet process were prevented. As shown in figure 6(*c*), the RIE (reactive ion etching) process was then used to remove the passivation layer to expose the metal bonding pads formed by the M4 layer. Finally, the Si substrate was etched isotropically using dry XeF_2 to suspend MEMS structures, as shown in figure 6(*d*).

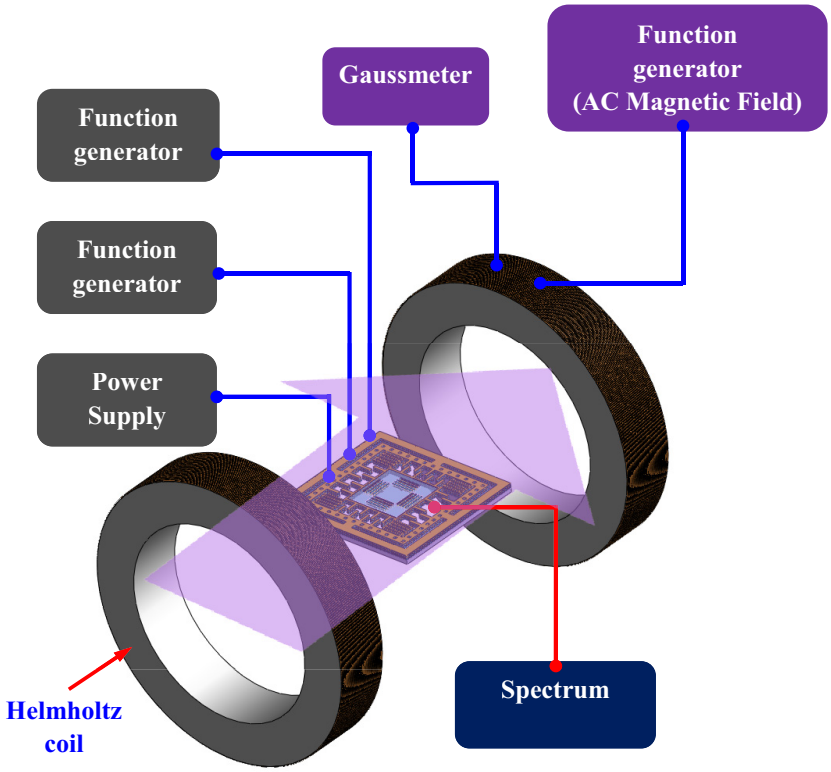

Figure 10. The measurement setup to characterize the performance of the packaged magnetic sensor. The input magnetic field was specified by the Helmholtz coils and calibrated by a commercial gauss meter. The function generator was employed to provide the modulation signal.

Figure 7 shows typical fabrication results. The scanning electron microscopy (SEM) micrograph in figure 7(*a*) shows a chip containing the typical fabricated three-axis magnetic sensor and its monolithically integrated sensing circuits. Moreover, a linear accelerometer is also monolithically integrated with the magnetic sensor on this chip. The zoom-in SEM micrograph in figure 7(*b*) shows the overview of a 600 μm $\times$ 580 μm suspended structure including springs, the proof-mass, the stress-compensation frame and sensing electrodes. As listed in table 1, the footprint of the proof-mass is 420 μm $\times$ 420 μm. The zoom-in SEM micrograph in figure 7(*c*) further depicts the two sets of in-plane magnetic coils embedded in the proof-mass. The M4 metal layers of the magnetic coils are observed from the micrograph, and each set of magnetic coil has 18 turns. The micrograph in figure 7(*d*) shows the sensing chip after wire bonding. Such a wire bonded chip is ready for tests. Figure 7(*e*) shows sensing electrodes in two different axes and the spring. The zoom-in micrograph in figure 7(*f*) indicates the electrodes with a sub-micron sensing gap.

4. Testing and results

The fabricated magnetic sensor was wire bonded and packaged in a ceramic house. After that, the measurement setup shown in figure 8(*a*) was established to characterize the temperature increase of the structure after applying currents to the magnetic coil. The temperature of the springs and proof-mass are increased by joule heat after applying currents to the magnetic coils and their electrical routings. Note that the input current on the magnetic coil is 6 mA during the operation of the sensor. The temperature distribution on the structure is characterized using the commercial infrared microscope with a spatial resolution of 3 μm and a temperature resolution of 0.1 °C. During the measurement, the sample was heated with a reference temperature of 70 °C provided by the infrared microscope [17]. Figure 8(*b*) shows the typical measured temperature distribution. It indicates that the springs for the current input to, and output from, the magnetic coils have the highest increasing temperature of less than 35 °C at 6 mA. The proof-mass with embedded magnetic coils has an increasing temperature of less than 5 °C at 6 mA. Moreover, the thermal deformations of the suspended structure at different input currents are characterized using the setup in figure 9(*a*). The out-of-plane bending deformation was measured using the optical interferometer. Figure 9(*b*) indicates the structure deformation characterized along the AA′ cross section on the proof-mass. Due to thin-film residual stresses, the radius of curvature (ROC) of the proof-mass is 3.19 mm when no current was applied on the coil. Due to the thermal expansion mismatch of thin films, the ROC of the proof-mass becomes 3.03 mm (∼5% change) at a 6 mA input current. Moreover, figure 9(*c*) shows the thermal deformation of the structure characterized along the BB′ cross section on the proof-mass. The ROC of the proof-mass changes from 3.02 mm (no current applied on the coil) to 2.78 mm at a 6 mA input current (∼8% change). According to the measurements in figure 8, the change of proof-mass ROC after driving at a 6 mA input current is mainly induced by the thermal deformation of the

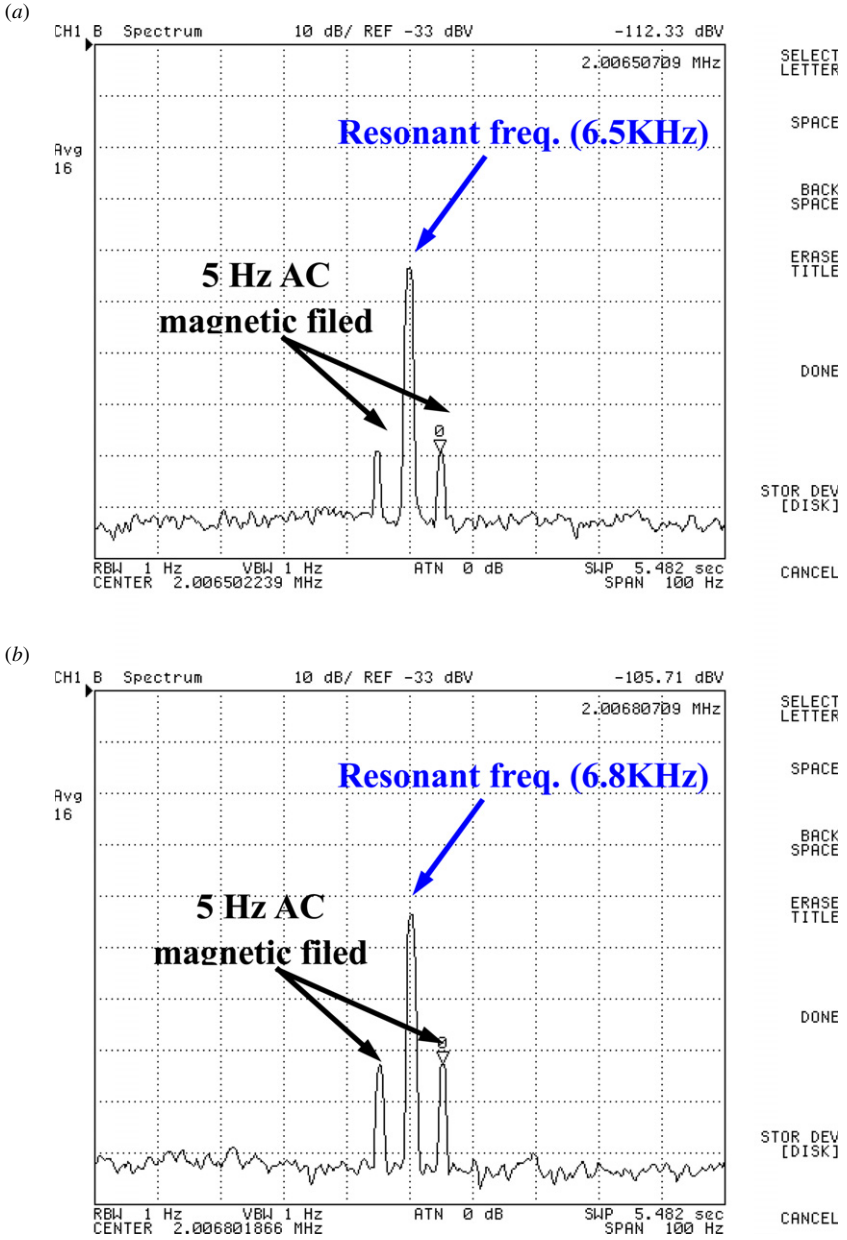

Figure 11. The typical frequency spectra in response to the signals detected from sensing electrodes after the sensor excited by (*a*) the *x*-axis in-plane magnetic field B_x (50 μT at 5 Hz) and (*b*) the *z*-axis out-of-plane magnetic field B_z (50 μT at 5 Hz).

springs. Moreover, the sensing area and sensing capacitance has a less than 1.4% variation caused by the change of the proof-mass ROC at a 6 mA input current.

This study established the measurement setup in figure 10 to characterize the performance of the packaged magnetic sensor shown in figure 7(*d*). The input magnetic field was specified by the Helmholtz coils and was calibrated by a commercial gauss meter. The function generator was employed to provide the modulation signal. In this study, the modulation signal was 1 Vpp at 2 MHz. Currents with a magnitude of 6 mA and frequencies of 6.5 kHz and 6.8 kHz were simultaneously applied to the magnetic-coils MC_x and MC_y. As discussed in section 2, these two frequencies are respectively the first two natural frequencies ω_x and ω_y of the spring–mass structure. To distinguish the sensing signals, a very low frequency magnetic field (5 Hz) was applied to the sensor when characterized by the spectrum analyzer [8]. The strength of the magnetic field was then determined by the intensity of the frequency response detected by the sensing electrodes. The typical measured frequency spectra in figure 11 are respectively in response to the in-plane (*x*-axis, B_x) and out-of-plane (*z*-axis, B_z) magnetic fields (50 μT at 5 Hz) specified by the Helmholtz coils. The frequencies of input currents 6.5 and 6.8 kHz are also respectively displayed by the peak of the spectra. The in-plane magnetic field (B_y) in the *y*-axis can also be detected by using the same manner. The measured noise floor in the frequency spectra indicates that the magnetic field resolutions of the presented sensor are respectively 384 nT rtHz^{-1} (*x*-axis), 403 nT rtHz^{-1} (*y*-axis) and 62 nT rtHz^{-1} (*z*-axis). The

Table 2. The detailed measurement results and the comparison with existing magnetic sensors.

Magnetic field axes detected by single proof-mass sensing unit	This study			[18]		[19]
	Three-axis			Two-axis		One-axis
	X	*Y*	*Z*	*X*/*Y*	*Z*	*X*/*Y*
Current (mA)	5.9	5.9	5.9	4.5	4.5	4.5
Sensitivity (μV μT^{-1})	0.21	0.20	0.90	0.92	3.20	20 000
Resolution (nT rtHz^{-1})	384	403	62	344	285	258
Resonant frequency (kHz)	6.5	6.8	6.5	117.4	40.5	16
Pressure	101 KPa (1 atm)			2 KPa		101 KPa (1 atm)
Quality factor	1.3			310	110	–
Size of MEMS structure (mm^2)	0.176			0.096		0.122

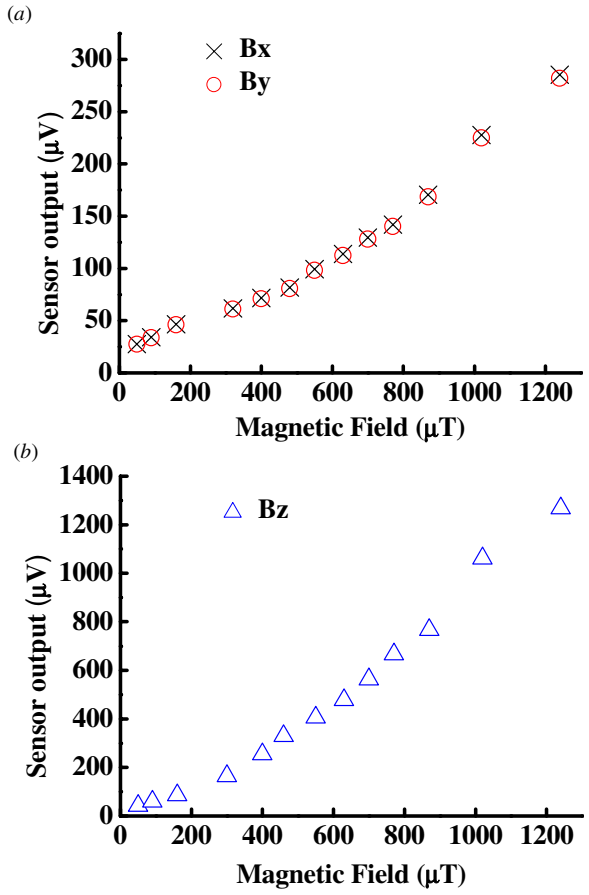

Figure 12. Variation of the output voltages from the magnetic sensor with the intensity of (*a*) the *x*-axis and *y*-axis magnetic fields, and (*b*) the *z*-axis magnetic field. The sensing range of the magnetic field is 0–1200 μT.

sensitivity of the presented sensors is determined after characterizing the output sensing voltages at magnetic fields of 0–1200 μT. Measurements in figure 12(*a*) respectively show the output voltages varying with the intensity of the *x*-axis and *y*-axis magnetic fields. The sensitivities of the magnetic sensor are respectively 0.21 μV μT^{-1} for B_x and 0.20 μV μT^{-1} for B_y. In addition, figure 12(*b*) shows the output voltages varying with the intensity of B_z, and the sensor has a sensitivity of 0.90 μV μT^{-1}. According to the simulation results, for the magnetic fields B_x (or B_y) and B_z of the same strength, the Lorentz force induced by B_z is larger than the electromagnetic force F_{EMx} (or F_{EMy}) introduced by B_x (or B_y). Thus, the spring mass structure has a larger dynamic response caused by the out-of-plane magnetic field B_z. As compared with the in-plane magnetic field B_x (or B_y), the magnetic sensor has a higher sensitivity for B_z. As discussed in [8], the sensitivity and resolution would be further improved while detecting the dc magnetic fields. Table 2 further summarizes the detailed measurement results and the comparison with the magnetic sensors in [18, 19]. The driving current could be reduced or the sensitivity could be further increased if the device were operating in a vacuum packaging with a higher quality factor.

5. Conclusions

In this study, a single unit three-axis magnetic sensor has been designed and implemented using the standard TSMC 0.35 μm 2P4M CMOS process. The magnetic sensor consists of springs, a proof-mass with embedded magnetic coils, and sensing electrodes. The metal and tungsten layers in the CMOS process have been employed to realize two sets of in-plane magnetic coils respectively aligned in two orthogonal axes. AC currents with two different frequencies respectively corresponding to the first two natural frequencies of the spring–mass structure are applied to the magnetic coils. The in-plane magnetic coils could respectively generate Lorentz and electromagnetic forces by out-of-plane and in-plane magnetic fields. Thus, the magnetic fields will introduce resonant vibrations of the spring–mass structure which are then detected by the capacitance sensing electrodes. Measurements on a typical fabricated magnetic sensor indicate the sensitivities for different axes are respectively 0.21 μV μT^{-1} for B_x, 0.20 μV μT^{-1} for B_y and 0.90 μV μT^{-1} for B_z at 1 atm. Moreover, the resolutions of the sensor are respectively 384 nT rtHz^{-1} for B_x, 403 nT rtHz^{-1} for B_y and 62 nT rtHz^{-1} for B_z at 1 atm. The sensitivity and resolution could be improved if the device were operated in a vacuum packaging with a higher quality factor. The presented three-axis magnetic sensor can further monolithically integrate with other CMOS-MEMS sensors using the same processes [14, 15, 17] for various applications.

Acknowledgments

This study is sponsored in part by the National Science Council of Taiwan under grant of NSC-102-2221-E-007-027-MY3,

NSC-102-2622-E-007-014, and NSC-102-2218-E-007-003-MY3. The authors appreciate support from the TSMC and the National Chip Implementation Center (CIC), Taiwan, for CMOS chip manufacturing. The authors wish to thank the Center for Nanotechnology, Material Science, and Microsystem of National Tsing Hua U and the National Nano Device Lab. in providing fabrication facilities. The authors would also like to thank the National Center for High-Performance Computing for the supporting of simulation tools.

References

[1] Honeywell, Inc. HMC5883L, three-axis digital compass IC www.magneticsensors.com/three-axis-digital-compass.php

[2] Asahi Kasei Microdevices Semicond. Inc. AK8975 3-axis electronic compass www.akm.com/akm/en/file/datasheet/AK8975.pdf

[3] Lenz J and Edelstein A S 2006 Magnetic sensors and their applications *IEEE Sensors J.* **6** 631–49

[4] Emmerich H and Schofthaler M 2000 Magnetic field measurements with a novel surface micromachined magnetic-field sensor *IEEE Trans. Electron Devices* **47** 972–7

[5] Bahreyni B and Shafai C 2007 A resonant micromachined magnetic field sensor *IEEE Sensors J.* **7** 1326–34

[6] Kyynäräinen J, Saarilahti J, Kattelus H, Kärkkäinen A, Meinander T, Oja A, Pekko P, Seppa H, Suhonen M and Kuisma H 2008 A 3D micromechanical compass *Sensors Actuators* A **142** 561–8

[7] Herrera-May A L, García-Ramírez P J, Aguilera-Cortés L A, Martínez-Castillo J, Sauceda-Carvajal A, García-González L and Figueras-Costa E 2009 A resonant magnetic field microsensor with high quality factor at atmospheric pressure *J. Micromech. Microeng.* **19** 015016

[8] Li M, Rouf V T, Thompson M J and Horsley D A 2012 Three-axis Lorentz-force magnetic sensor for electronic compass applications *J. Microelectromech. Syst.* **21** 1002–10

[9] Wattanasarn S, Matsumoto K and Shimoyama I 2013 3D Lorentz force magnetic sensor using ultra-thin piezoresistive cantilevers *Proc. 26th IEEE Int. Conf. Micro Electro Mech. Syst. (Taipei, Taiwan, 20–24 Jan.)* pp 693–6

[10] Fedder G K, Howe R T, King Liu T-J and Quevy E P 2008 Technologies for co-fabricating MEMS and electronics *Proc. IEEE* **96** 306–22

[11] Eyre B, Pister K S J and Kaiser W 1998 Resonant mechanical magnetic sensor in standard CMOS *IEEE Electron Device Lett.* **19** 496–8

[12] Beroulle V, Bertrand Y, Latorre L and Nouet P 2003 Monolithic piezoresistive CMOS magnetic field sensors *Sensors Actuators* A **103** 23–32

[13] Chang C-I, Tsai M-H, Liu Y-C, Sun C-M and Fang W 2013 Development of multi-axes CMOS-MEMS resonant magnetic sensor using Lorentz and electromagnetic forces *Proc. 26th IEEE Int. Conf. Micro Electro Mech. Syst. (Taipei, Taiwan, 20–24 Jan.)* pp 193–6

[14] Liu Y-C, Tsai M-H and Fang W 2012 Pure oxide structure for temperature stabilization and performance enhancement of CMOS-MEMS accelerometer *Proc. 25th Int. Conf. on Micro Electro Mechanical System (Paris, France, 29 Jan.–2 Feb.)* pp 591–3

[15] Sun C-M, Tsai M-H, Liu Y-C and Fang W 2010 Implementation of a monolithic single proof-mass tri-axis accelerometer using CMOS-MEMS technique *IEEE Electron Device Lett.* **57** 1670–9

[16] Tsai M-H, Sun C-M, Liu Y-C, Wang C and Fang W 2009 Design and fabrication of a metal wet-etching post-process for the improvement of CMOS-MEMS capacitive sensors *J. Micromech. Microeng.* **19** 105017

[17] Quantum Focus Instruments Corporation *QFI InfraScope II, InfraScope User's Manual* http://mntl.illinois.edu/Equipment/docs/InfraScopeManual.pdf

[18] Rouf V T, Li M and Horsley D A 2013 Area-efficient three axis MEMS Lorentz force magnetometer *IEEE Sensors J.* **13** 4474–81

[19] Alandry B, Latorre L, Mailly F and Nouet P 2011 A fully integrated inertial measurement unit: application to attitude and heading determination *IEEE Sensors J.* **11** 2852–60